MATERIALS SCIENCE

Stretchable photothermal membrane of NIR-II charge-transfer cocrystal for wearable solar thermoelectric power generation

Yu Dong Zhao[1]†, Wangkai Jiang[2]†, Sheng Zhuo[3]†, Bin Wu[1,4], Peng Luo[1], Weifan Chen[3], Min Zheng[2], Jianchen Hu[2], Ke-Qin Zhang[2]*, Zuo-Shan Wang[1]*, Liang-Sheng Liao[4]*, Ming-Peng Zhuo[2,4]*

Harvesting sunlight into cost-effective electricity presents an enticing prospect for self-powered wearable applications. The photothermal materials with an extensive absorption are fundamental to achieve optical and thermal concentration of the sunlight for efficiency output electricity of wearable solar thermoelectric generators (STEGs). Here, we synthesize an organic charge-transfer (CT) cocrystal with a flat absorption from ultraviolet to second near-infrared region (200 to 1950 nanometers) and a high photothermal conversion efficiency (PCE) of 80.5%, which is introduced into polyurethane toward large-area nanofiber membrane by electrospinning technology. These corresponding membranes demonstrate a high PCE of 73.7% under the strain more than 80%. Sandwiched with carbon nanotube–based thermoelectric fibers, the membranes as stretchable solar absorbers of STEGs could supply a notably increase temperature gradient, processing a maximum output voltage density of 23.4 volts per square meter at 1:00 p.m. under sunlight. This strategy presents an important insight in heat management for wearable STEGs with a desired electricity output.

INTRODUCTION

Wearable solar thermoelectric generators (STEGs) have generated immense scientific interest owing to their desired capacity for electricity generation via energy harvesting from both light and heat without greenhouse gas emissions (*1*). The healable thermoelectric generators (TEGs) assembled from commercial Bi_2Te_3 and Sb_2Te_3 thermoelectric (TE) legs could generate a superior output power of 8.0 mW with a temperature gradient of 20 K (*2*). In addition to the outstanding TE materials, tremendous efforts have been made to increase temperature gradient across the TE yarns for the high-efficiency energy conversion from thermal to electricity according to the Seebeck effect (*3*). Representative cases were realized via optimizing the thermal impedance (*4*) and regulating the temperature of the cold or hot surfaces, including heat sink (*5*), circulation water (*6*), and appropriate air velocities (*7*). However, these successes generally suffer high cost, sophisticated process, and bulky instruments, terribly limiting their practical applications. Photothermal materials are promising alternatives for environmentally friendly thermal management via efficiently harvesting solar energy for heat, which contributes to the elevated temperature gradient for a preferable electricity generation (*8*, *9*).

Organic semiconductors with tailor-made molecular structures (*10*), low-temperature solution processing (*11*), and high compatibility with plastic substrates (*12*) are emerging as considerable building blocks of photothermal materials for photoacoustic imaging (*13*), solar desalination (*14*), and photothermal-electric devices (*15*). To meet practical requirements of high photothermal conversion efficiency (PCE), considerable endeavors have been devoted to increasing absorption ability from ultraviolet (UV) to near-infrared (NIR) region, especially second NIR (NIR-II) region. Representative cases include incorporating free radicals into films (*16*), using host-guest complexation (*17*) to stabilize photothermal radicals, or introducing intramolecular CT in conjugated molecules (*18*). Nevertheless, the complicated design, the tedious preparation, or the restricted absorption below NIR-II region was inescapability found in these methods for polymers (*13*), organic radicals (*19*), and small organic molecules (*20*). Organic charge-transfer (CT) cocrystals could subtly generate impressive optoelectronic properties over their components through a simply self-assembly process of electron donors and acceptors, such as optical waveguide (*21*), stimuli responsiveness (*22*), and room-temperature ferroelectricity (*23*). Substantially, the unique orbital hybridization of organic CT cocrystals caused by the electron delocalization from the donor to the acceptor is important to obtain the impressive red-shift in absorption, benefiting for the high PCE (*24*). However, the limited CT cocrystals with NIR-II absorption have largely remained a case-by-case practice with ambiguous regulation mechanism, as well as the lack of systematic theoretical summary (*25*). It reveals that fabricating a CT cocrystal with NIR-II absorption is rather challenging. Notably, the controlled electron delocalization by the spatial arrangement and the multiple intermolecular interactions between elaborately selected units are potential criterions for designing NIR-II absorption organic photothermal materials (*26*). Compared with the photothermal mono-molecules with NIR-II absorption, the cocrystal engineering supplies a facile and universal approach to design the desired organic functional materials. Specifically, the appropriate energy structure matching and the intense electron-donating/withdrawing ability of constituents are crucial for rational design of the desired organic photothermal CT

[1]College of Chemistry, Chemical Engineering and Materials Science, Soochow University, Suzhou 215123, China. [2]College of Textile and Clothing Engineering, Soochow University, Suzhou 215123, China. [3]School of Physics and Materials Science, Nanchang University, Nanchang 330031, China. [4]Institute of Functional Nano and Soft Materials (FUNSOM), Soochow University, Suzhou 215123, China.
*Corresponding author. Email: mpzhuo@suda.edu.cn (M.-P.Z.); kqzhang@suda.edu.cn (K.-Q.Z.); zuoshanwang@suda.edu.cn (Z.-S.W.); lsliao@suda.edu.cn (L.-S.L.)
†These authors contributed equally to this work.

cocrystals. Furthermore, the electrospinning technology demonstrated the controllable morphology and excellent stretchability, inducing an immense advantage for forming the large-area nanofiber membrane of NIR-II absorption CT cocrystal (*24*). These flexible nanofiber membranes supply an opportunity as full-spectrally solar absorbers layer for high thermal concentration, which could increase the temperature gradient of wearable STEGs and power a large electricity generation.

Here, we purposefully selected the electron donor *N*,*N*,*N*′,*N*′-tetramethylbenzidine (TMBD) and electron acceptor tetrachloro-1,4-benzoquinone (TCBQ) to prepare the organic photothermal cocrystals via a facile solution-evaporation process. The notable orbital hybridization between TMBD and TCBQ could rationally design the narrow energy gap of 1.5 eV and a broad absorption spectrum from 200 to 1950 nm. The high PCE (80.5%) of the TMBD-TCBQ (TTC) cocrystal attributes to the rapid nonradiative transitions of the excited CT state as verified by the femtosecond transient absorption (Fs-TA) spectroscopy. We successfully introduced TTC cocrystal into polyurethane (PU) to form a stretchable photothermal nanofiber membrane via a cost-effective electrospinning technology, which processes a high PCE of 73.7% at even 80% strain. Furthermore, using these photothermal nanofiber membranes as optical concentrators via coating on the surface of the carbon nanotube (CNT)–based TE fibers efficiently increases temperature gradient of 33°C for high electricity generation. Typically, these wearable STEGs achieved a maximum output voltage density of 23.4 V/m^2 at 1:00 p.m. under natural light. This work promotes the progress of organic photothermal conversion materials in the NIR-II window and provides a delicate avenue for high TE performance wearable electronics.

RESULTS

Design and preparation of TTC cocrystal microrods

The representative planar aromatic molecule of TMBD with a large π-conjugated structure could controllably self-assemble into one-dimensional (1D) microrods via π-π interactions, which demonstrated intense blue emission with a photoluminescence (PL) peak at 415 nm (Fig. 1A$_1$ and fig. S1). To further perceive the electron attraction or repulsion ability, electrostatic potential (ESP) analysis was conducted as a quantitative parameter to investigate the relationship between molecular structure and intermolecular interactions (Fig. 1A) (*27*). The negative ESP values occupying a majority surface of the TMBD demonstrate its strong electron-donating ability, which is favorable for constructing the organic CT cocrystal via CT interaction (*28*). The positive ESP values of the TCBQ surface illustrate its intense electron-withdrawing property ascribed to the chlorine atom, which is widely applied as a strong electron acceptor for forming organic CT cocrystals (*29*). In this regard, TMBD and TCBQ were used to rationally design and synthesize TTC CT cocrystals via a self-assembly process (*30*, *31*). Owing to the strong CT interaction, TMBD and TCBQ could self-assemble into 1D microrods with no emission, in contrast with the blue-emissive TMBD microrods and the non-emissive TCBQ microplates (Fig. 1, A$_2$ and A$_3$, and fig. S1). The prepared TTC cocrystal single crystal appears dark black in color with a metallic luster and displays an impressive difference from its components (fig. S2), which is agreed with the single-crystal data (a = 8.427 Å, b = 8.938 Å, c = 7.932 Å, α = 93.36°, β = 109.60°, and γ = 72.22°) (table S1). These results are powerful for confirming the fabrication of TTC cocrystals. The scanning electron microscopy (SEM) and transmission electron microscopy (TEM) images (Fig. 1, B and C) demonstrate the typical 1D structure of the TTC cocrystal microrods with a smooth surface, which is in accord with the simulated growth morphology (inset of Fig. 1B). Impressively, the shiny and clear diffraction points of the selected area electron diffraction (SAED) pattern (Fig. 1C) suggest the high crystallinity of these prepared TTC microrods, which agrees with the intense and distinct characteristic diffraction peaks of the x-ray diffraction (XRD) pattern (Fig. 1D). The SAED pattern with a measured d-spacing value of 2.1 Å could be indexed to the (040) crystal plane, suggesting that the high-quality TTC microrods grow along the direction of [010] with a face-to-face mode packing arrangement (lower left inset of Fig. 1C and table S2). Moreover, the XRD pattern of the TTC cocrystal microrods is distinct from that of each constituent monomer, as verified in Fig. 1D, and the diffraction peaks of the (010), (110), and (020) planes are consistent with the exposed crystal planes in the simulated growth morphology (inset of Fig. 1B). As depicted in Fig. 1E and fig. S3, the calculated functions of the reduced density gradient and Sign(λ_2)ρ illustrate intermolecular noncovalent interactions in TTC cocrystal microrods. Typically, the green region indicates impressive attractive interactions, and the brown region implies large steric hindrance (*32*). From the quantitative perspective, the distances of TMBD-TCBQ and TMBD-TMBD as determined from the crystal packing structures are 3.299 and 3.347 Å, respectively, which demonstrate the intense CT interaction and strong intermolecular π-π interaction (Fig. 1F and figs. S4 and S5). Furthermore, the calculated distance of the C—H···Cl hydrogen bond is 2.939 Å, and the proportion is 35.7% based on the Hirshfeld surface (figs. S6 and S7), where the full fingerprints are displayed as gray shadows and the pointing interactions appear as blue (*33*). Notably, the mixed stacking arrangement and the multiple noncovalent interactions contribute to stimulating intramolecular vibrations. It dissipates the energy of the excited molecules and facilitates efficient fluorescence quenching (fig. S1) (*34*). All these results confirm the successful fabrication of organic TTC microrods through a convenient solution self-assembly process.

Characteristics of CT nature

Multiple depictions of the CT nature between TMBD and TCBQ have been performed. Compared with the inconspicuous results of individual TMBD and TCBQ in electron spin resonance (ESR) (Fig. 2A), these prepared TTC microrods present an impressive resonance signal, which is in accordance with the character of the CT interaction in the ground state (*35*). Furthermore, the corresponding g value of 2.0067 approaches the factor of free electrons (2.0032), which illustrates the presence of unpaired electrons in TTC microrods and the CT from TMBD to TCBQ (*31*). As depicted in the Raman spectra (Fig. 2B), the sharp bands demonstrate that the TTC cocrystal microrods are highly crystalline and composed of TMBD and TCBQ (*36*). The characteristic peaks at 1603 cm^{-1} of TMBD and TCBQ owing to the C═C stretching vibrations are shifted to 1585 cm^{-1} in TTC microrods, which confirms that the electron cloud density of the benzene ring could be strengthened by the cocrystal strategy (*37*). The peak at 949 cm^{-1} ascribed to the weak antisymmetric NC$_2$ stretching of TMBD is blueshifted to 982 cm^{-1} in TTC microrod, which demonstrates the impressive

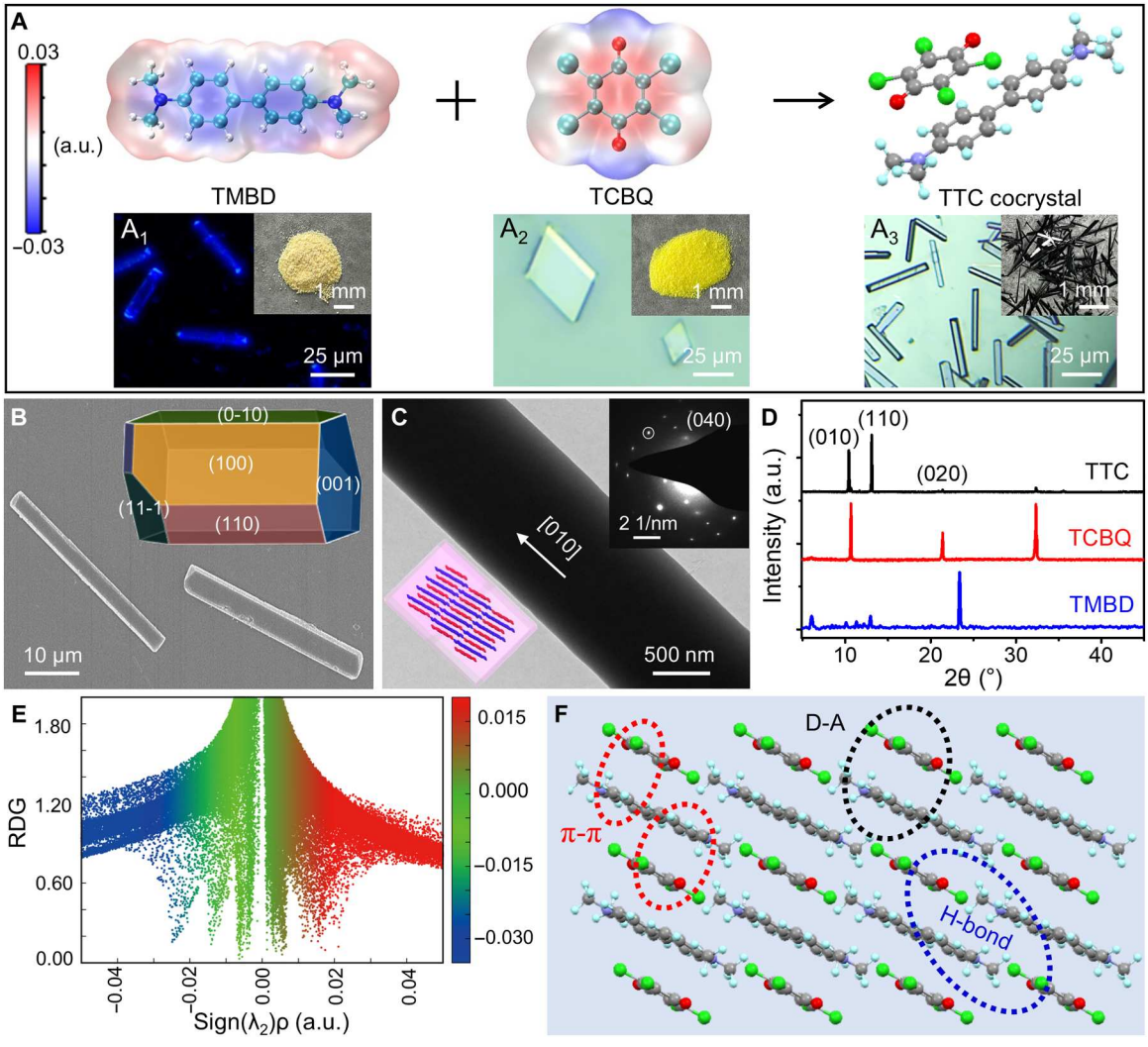

Fig. 1. Design and syntheses of organic cocrystal. (**A**) Electrostatic potential (ESP) maps, molecular structure, and cocrystallization of TMBD, TCBQ, and TTC cocrystals, together with corresponding FM and bright optical images. Scale bars, 25 μm. Top right inset of (A_1) to (A_3): The corresponding powders. Scale bars, 1 mm. (**B**) Scanning electron microscopy (SEM) image of TTC cocrystal microrods. Scale bar, 10 μm. Inset: The corresponding simulated growth morphology. (**C**) Transmission electron microscopy (TEM) image of the individual TTC cocrystal microrod. Scale bar, 500 nm. Top right inset: The corresponding selected area electron diffraction (SAED) pattern of this cocrystal microrod. Scale bar, 2 1/nm. Bottom left inset: The corresponding mixed packing model. (**D**) The x-ray diffraction (XRD) characterizations of TMBD powders, TCBQ powders, and TTC cocrystal microrods. (**E**) Calculated functions of reduced density gradient (RDG) and Sign(λ_2)ρ for TTC cocrystal microrods. (**F**) Crystal stacking of the TTC cocrystal microrods.

CT process between TMBD and TCBQ. As shown in the Fourier transform infrared (IR) spectra (Fig. 2C), the characteristic peaks at 1346 and 1508 cm^{-1} of TMBD could be assigned to C─H and N─H stretching vibrations of a tertiary amine, which are blueshifted to 1359 and 1510 cm^{-1} in TTC microrods. The characteristic peak at 1683 cm^{-1} of TCBQ ascribed to C═O stretching vibrations is redshifted to 1660 cm^{-1} in TTC microrods. These results powerfully demonstrate the substantial CT process from TMBD to TCBQ (*34*). From the solid-state ^{13}C nuclear magnetic resonance (NMR) spectroscopy (Fig. 2D and fig. S8), the TCBQ chemical shift at 138.8 parts per million (ppm) moves to 133.4 ppm in TTC microrods. In addition, the TMBD chemical shift at 38.9 ppm (124.5 ppm) moves downfield 39.3 ppm (125.9 ppm) in TTC microrods. These chemical shift patterns imply a reduction in the π-electron density on the conjugated system of TMBD and an increase in the electron density on the benzene ring of TCBQ after cocrystallization. This further clarifies that the direction of the CT process is from TMBD to TCBQ (*36*). As illustrated in Fig. 2E, TTC microrods display a large and favorable absorption from the UV to NIR-II region, agreeing with the narrow bandgap of 1.5 eV. Compared to the absorption below 500 nm of individual TMBD and TCBQ, the broad absorption of TTC microrods further corroborates the strong CT interaction between TMBD and TCBQ. Furthermore, as given in the energy diagrams, the highest occupied molecular orbital (HOMO) of the TTC cocrystal at −4.79 eV nears the TMBD HOMO of −4.42 eV, and the lowest unoccupied molecular orbital (LUMO) of the TTC cocrystal at −3.29 eV approaches the TCBQ LUMO of −4.20 eV, extending its absorption from 200 to 1950 nm. On the basis of

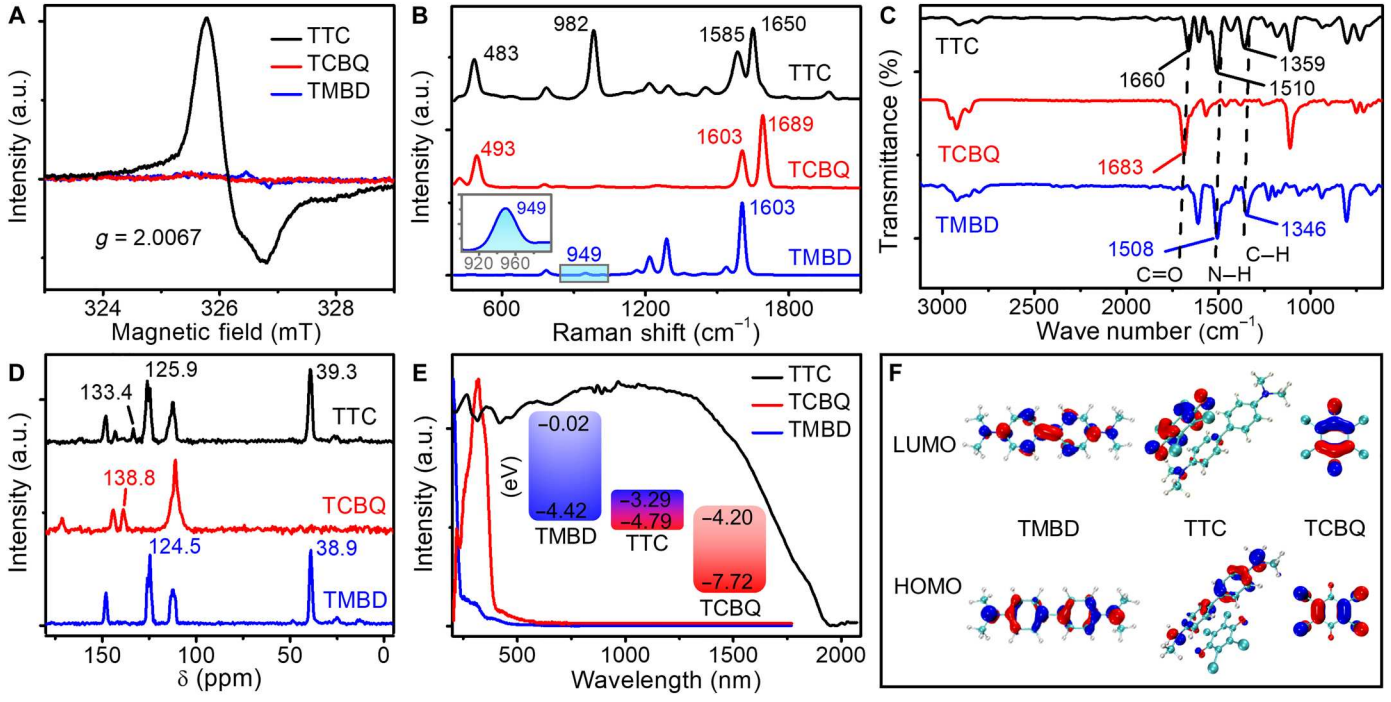

Fig. 2. Characteristic of CT nature. (**A**) Electron spin resonance (ESR) spectra, (**B**) Raman spectra, (**C**) Fourier transform infrared spectra, and (**D**) solid-state ^{13}C nuclear magnetic resonance (NMR) spectra of TMBD, TCBQ, and TTC cocrystal microrods. (**E**) Absorption spectra of TMBD, TCBQ, and TTC cocrystal microrods. Inset: The calculated energy diagrams. (**F**) Molecular orbital (MO) diagrams of TMBD, TCBQ, and TTC cocrystal microrods.

orbital hybridization (Fig. 2F), the CT process goes from the HOMO of TMBD to the LUMO of TCBQ, and the electron cloud is rearranged to form impressive molecular orbitals (MOs) wherein the cocrystal HOMO is distributed on the TMBD and its LUMO is focused on the TCBQ (*38*).

Investigation on photothermal properties and mechanism

The broad and strong absorption of these prepared TTC microrods is beneficial for high-efficiency photothermal conversion. Under 808-nm laser irradiation with a power density of 0.287 W/cm^2 for 20 s, the temperature of the TTC microrods markedly increases from 31.9° to 86.0°C and then reaches relative equilibrium, as depicted in Fig. 3A. In contrast, the temperature of pure TMBD and TCBQ microcrystals is negligibly enhanced. Notably, the TTC microrods demonstrated a high PCE of 80.5% compared with that of reported organic photothermal CT cocrystals as depicted in table S3, which was calculated according to the linear relationship between cooling time and ln(θ) via the previous method (fig. S9) (*39*). The dimensionless temperature θ represents the ratio of the temperature change to the maximum temperature change. While increasing the power density from 0.116 to 0.287 W/cm^2, the maximum temperatures increase from 55.1° to 86.0°C (Fig. 3B), suggesting a typical power density–dependent photothermal characteristic. As shown in Fig. 3C, the temperature variations are proportional to the different NIR light excitation power densities in the heating and cooling processes during 0 to 700 s. The maximum temperature is in keeping with that in Fig. 3B, suggesting the outstanding power density dependence and photostability of TTC microrods. Under 808-nm laser illumination, the IR images of TTC microrods become increasingly bright with increasing irradiation time from 5 to 60 s and the power densities from 0.116 to 0.287 W/cm^2 (Fig. 3D). It reveals potential applications in time-resolved responses and photothermal imaging (*34*). As shown in Fig. 3E and fig. S10A, the corresponding linear relationship between ΔT and the power densities implies that the temperature could be subtly controlled by changing the excitation power densities. After undergoing heating and cooling cyclic tests under 808-nm laser irradiation with a power density of 0.287 W/cm^2, the maximal temperature of TTC microrods remains at approximately 86°C (Fig. 3F). Combined with the constant temperature in other power density cyclic tests (fig. S10), this result impressively illustrates the splendid photothermal stability of TTC microrods.

To better comprehend the underlying mechanism of the nonemissive behaviors and the excellent photothermal performance of TTC microrods, Fs-TA spectra were implemented to elucidate excited state relaxation dynamics. As shown in fig. S11, after 808-nm light excitation, a broad absorption band centered at 480 nm immediately emerges with a delay time of 0.12 ps, whose intensity improves from 0.12 to 0.31 ps due to the excited CT state (*40*). As the delay time further increases from 0.31 to 66.8 ps, the positive absorption peak gradually weakens and even disappears at 2.49 ns, which stems from the rapid deactivation of the excited CT state via the nonradiative transitions of the internal conversion (IC) process from CT_n to CT_1, dissociation into the charge-separated (CS) state, and the excited polaron decaying undergoing the IC pathway to the ground state (*41*, *42*). Furthermore, the kinetics at 482 nm could be fitted appropriately by a three-exponential function with time constants of τ_1, τ_2, and τ_3. The corresponding first decay lifetime τ_1 of 0.48 ps (59.5%) reveals the IC process from excited state $^1CT_1$ to ground state CT_0. Notably, the predominant

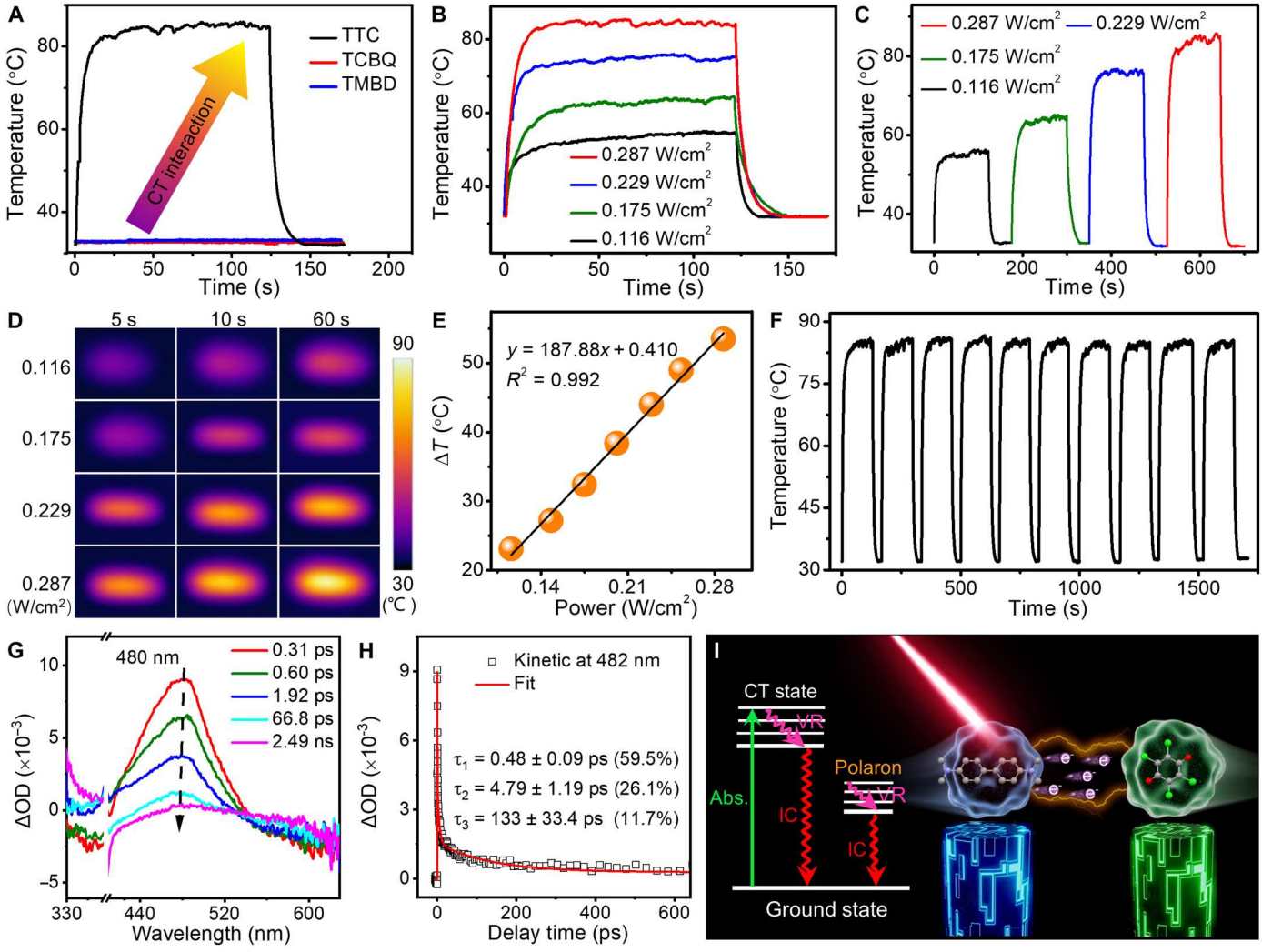

Fig. 3. Photothermal performance of TTC microrods under 808-nm laser illumination and investigation on photothermal mechanism. (**A**) Temperature variations of the TTC microrods, TCBQ, and TMBD with a power density of 0.287 W/cm^2. (**B**) Temperature variations of TTC microrods with different power densities. (**C**) Temperature variations of TTC microrods at varied power densities of heating and cooling processes. (**D**) IR images of TTC microrods corresponding to different illumination times and power densities. (**E**) Linear relationship between ΔT and the different power densities. (**F**) Ten heating and cooling cyclic tests of TTC microrods with a power density of 0.287 W/cm^2. (**G**) Fs-TA spectra of TTC microrods from 0.31 ps to 2.49 ns. Optical density, OD. (**H**) Kinetic fitting results of the TTC microrods at 482 nm. (**I**) Jablonski diagram of TTC microrods.

IC process accelerates molecules to achieve the energy dissipation cycles of excited states (*41*). The second lifetime τ_2 of 4.79 ps (26.1%) indicates that the CTs to the CS state and then back to the ground state through IC. The last lifetime τ_3 of 133 ps (11.7%) illustrates the polaron decaying and then back to the ground state through IC, which contributing to the thermal generation (*42*). The Jablonski diagram of TTC microrods in Fig. 3I illustrates the photophysical processes of the photothermal conversion on the basis of the excited state decay dynamics. First, electrons occur between these notable MOs from the ground CT (CT_0) state to excited CT (CT_n) states with light excitation. After that, the excited electrons and polaron pairs will experience nonradiative dynamic processes of IC, charge dissociation, and polaron decaying, eventually returning to the ground state. Substantially, the excitons all meet at the CT_n state of the TMBD-TCBQ on account of the formation of the impressive MOs, which results in the absence of optical transitions for the blue emission of the pure TMBD molecule. Consequently, these nonradiative decay processes favor excellent photothermal conversion properties via subtle organic CT cocrystal engineering (*31*, *34*).

Photothermal conversion of stretchable photothermal nanofiber membrane

PU with high tensile strength and elasticity was used to construct the desired matrix of the photothermal nanofiber membrane, which was named the TTC-PU photothermal membrane. As depicted in the SEM image (Fig. 4A), the prepared nanofiber demonstrates a smooth surface and uniform diameter. Moreover, electrospinning realizes the manufacture of a large-area membrane (8 cm by 24 cm) with a light brown color and smooth surface (inset of Fig. 4A). To further investigate its photothermal properties, an experiment was conducted under a xenon (Xe) lamp whose entire

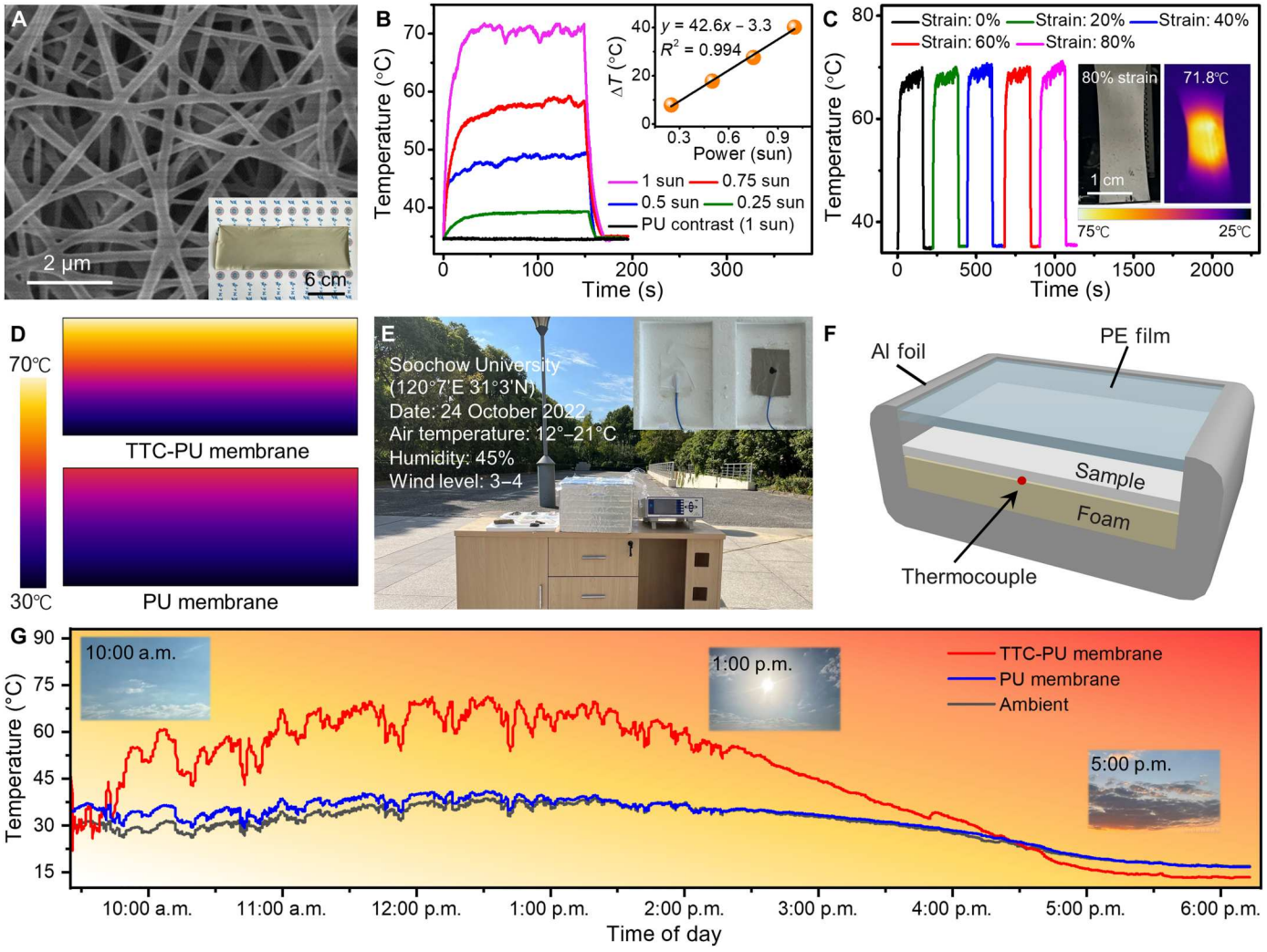

Fig. 4. Fabrication and photothermal properties of stretchable TTC-PU photothermal nanofiber membrane. (**A**) SEM image of the TTC-PU membrane. Scale bar, 2 μm. Inset: Optical image of the TTC-PU membrane. Scale bar, 6 cm. (**B**) Temperature variations of the TTC-PU membrane under different Xe light intensities and of the PU membrane under 1-sun Xe light intensity. (**C**) Temperature variations of the TTC-PU membrane under 0 to 80% strain illuminated by 1-sun Xe light intensity. Inset: Optical and IR images of the TTC-PU membrane under 80% strain illuminated by 1-sun Xe light intensity. Scale bar, 1 cm. (**D**) Comparison of the photothermal effect of the TTC-PU membrane and the PU membrane simulated by COMSOL. (**E**) Meteorological and topographic information of the experimental locations. Inset: Optical images of the tested PU membrane (white) and TTC-PU membrane (light brown). (**F**) Schematic diagram of the installation for investigating the outdoor photothermal performance. (**G**) The recorded real-time temperature of the TTC-PU membrane, PU membrane, and ambient environment under natural light.

light spectrum is close to that of the sun. As shown in Fig. 4B, when increasing the Xe light intensity from 0.25 to 1 sun, the maximum temperatures sharply increase from 39.4° to 71.8°C, in contrast with the changeless temperature of the pristine PU membrane. In addition, the IR images of the TTC-PU photothermal membrane become brighter and clearer with increasing illumination time and intensity of Xe light, which confirms its fast and sensitive photothermal response (fig. S12). The PCE of the TTC-PU photothermal membrane is 73.7% according to the linear relationship between the cooling time and ln(θ) (fig. S13) (*39*). The good linear relationship between ΔT and different sun intensities for the TTC-PU photothermal membrane (inset of Fig. 4B) provides a facile method to enhance the photothermal performance by modulating the sun intensities. As shown in figs. S14 and S15, multiple heating and cooling cyclic measurements under different Xe light intensities were conducted, powerfully confirming the excellent photostability of the TTC-PU photothermal membrane. The 6-hour continuous irradiation and 60 on/off cycles deeply demonstrate the splendid photostability of TTC cocrystal microrods, as well as their composite nanofiber membranes (fig. S16). To further verify the stability, the absorption spectra of the TTC-PU photothermal membrane under different situations were measured (fig. S17). Impressively, the properties of light absorption have not changed either in contact with the aqueous solution or after a month of storage. As depicted in fig. S18A, the tensile strength increases from 0 to 22.79 kPa, and the elongation at break is up to 82%. This confirms the desired flexibility and stretchability of the TTC-PU photothermal membrane. Under different tensile strain states from 0 to 80% with 1-sun Xe light irradiation, the maximum temperatures of the prepared TTC-PU photothermal

membrane all reach nearly 82°C (Fig. 4C). It is profoundly illustrated that tensile deformation has almost no impact on the TTC-PU photothermal membrane. The IR and optical images of the TTC-PU photothermal membrane stretched at 80% strain simultaneously demonstrate the splendid photothermal conversion and mechanical flexibility (inset of Fig. 4C), in contrast to the original shape in fig. S18B. The TTC cocrystals coated in PU could achieve a controlled self-assembly process. Owing to the protection of the PU substrate for the TTC cocrystals, these stretchable photothermal performances could not be influenced by the size (figs. S19 and S20) (*43*, *44*). As depicted in Fig. 4D and fig. S21, theoretical simulations were constructed by COMSOL to further affirm the reliability of the experimental data. The photothermal effects of the test group (TTC-PU photothermal membrane) and the control group (PU membrane) were simulated through the heat transfer module of COMSOL (*45*). A mass of solar radiation could be absorbed by the TTC-PU photothermal membrane, which contributes much higher temperature than the PU membrane in the case of direct sunlight (600 W/m^2).

Moreover, the temperature of the TTC-PU photothermal membrane was continuously monitored by carrying out outdoor experiments in Suzhou (China) on 24 October 2022 (Fig. 4E). The practical weather was cloudless and sunny (12° to 21°C) with suitable humidity (45%) and low wind (wind level of 3 to 4). As displayed in Fig. 4F, the installation consists of an expanded polystyrene shell, which is covered with a layer of aluminum (Al) foil to reflect radiation from the outside environment. The TTC-PU photothermal membrane and the pure PU membrane were placed on the foam-insulated sample table, which were both covered with a layer of IR-transparent wind cover polyethylene film. Moreover, thermocouples were placed between the sample and the sample table to record the temperature. The temperature variation of the TTC-PU photothermal membrane is consistent with the sunlight intensity (Fig. 4G). Impressively, the corresponding temperature rises to a maximum of 71.3°C at noon (11:30 a.m. to 1:30 p.m.), when the solar radiation is at its strongest in 1 day. However, the temperatures of the PU membrane and the ambient environment reach 41° and 38.7°C, respectively. Another cloudy day on 2 November 2022 was chosen to carry out the photothermal test with a solar power meter (fig. S22). The temperature of the TTC-PU photothermal membrane could rise to a maximum of 63.7°C under a peak solar irradiance of approximately 100 mW/cm^2 at 12:50 p.m., in contrast with 35.9° and 30.4°C for the PU membrane and ambient conditions, respectively. The consistency between the temperature evolution of the TTC-PU photothermal membrane and solar radiation demonstrates the fast response to natural light. The TTC-PU photothermal nanofiber membrane shows great potential for wide utilization in the fields of photoelectric products owing to its considerable photothermal stability, durability, flexibility, light weight, and large area.

Manufacture and power generation of wearable STEG

The pristine CNT yarns with an average diameter of ~105 μm demonstrated high TE performance, flexibility, and scalability (*3*), which are favorable P-type TE elements (table S4). To obtain the N-type TE elements, the CNT yarns were chemically treated with polyethyleneimine (PEI) on one side, which has been widely used for N-type doping of CNT yarns (*46*). The output voltages of single p-type and n-type linearly varying with temperatures were depicted in fig. S23A. The high Seebeck coefficient of single P-N pair is calculated to be 130 μV/K according to the fig. S23B. After stored ambient conditions for 25 weeks, these CNT P-N pairs still maintain a stable Seebeck coefficient of 130 μV/K (fig. S24), which confirms the effective and stable features of the corresponding physical adsorption. The dragon skin was used as the flexible elastomeric substrate of 6 cm by 4 cm by 1.2 cm (length by width by height) to hold CNT-based TEG upright in a practical direction for the heat flow (Fig. 5A). As depicted in fig. S25, the highly integrated TEG was prepared by assembling approximately 100 units of CNT yarns from five sets of the above configuration. The TE properties of the flexible CNT-based TEG within a small area of 24 cm^2 were investigated. As depicted in Fig. 5B, the output voltage increases linearly with P-N pairs and ΔT. The maximum output voltage reaches 71 mV with 81 pairs and a ΔT of 9.2°C. The variations in output power density along with external resistance at different ΔT are shown in fig. S26, which indicates that adjusting the external resistance until it equals the internal resistance could obtain the maximum power density. Impressively, the maximum output power density is 120 μW/m^2 at ΔT = 11.8°C when the external resistance is 7662 ohms. The output power density and the circuit current of the TEG as functions of the output voltage at different ΔT are displayed in Fig. 5C. The TEG with the maximum power density at ΔT = 11.8°C processes a circuit current of 6.33 μA and an output voltage of 47.4 mV. The schematic in Fig. 5D depicts the effective method to improve the TE power generation of TEG by introducing the TTC-PU photothermal membrane, which is beneficial for the high operation ΔT. The TTC-PU photothermal membrane was directly stickied to the CNT-TEG, which is owing to the strong adhesion of the dragon skin (fig. S27). The desired contact is conducive to the successful established temperature gradient without any influence on output voltage, which promotes the stability of TE performance. Moreover, the flexible simulated skin is composed of a silicone rubber–insulated heater with a constant input power (104 W/m^2), which is regarded as the cold side of 37°C. Notably, the CNT yarns could absorb the solar light while would not influence the TE generator performance, owing to the impressive photothermal impact originated from the excellent optical concentrators of TTC-PU membrane (figs. S28 and S29). The TTC-PU membrane with a broad NIR-II absorption from 200 to 1950 nm coved on CNT yarns could absorb most of the solar light, which would restrain the photothermal effect of CNT yarns. To further test the desired influence of the TTC-PU photothermal membrane on TEG, the voltage density generated by the TE device was investigated under irradiation by Xe light. As illustrated in Fig. 5E, the voltage density without the membrane is negative at the beginning. In contrast, the voltage density of the TE device covered with the TTC-PU photothermal membrane immediately increases to a positive value under different Xe light intensities. The successful formation of a larger temperature gradient and the fabrication of flexible wearable TEG (TTC-STEG) based on the TTC-PU photothermal membrane are demonstrated in detail. Moreover, the maximum voltage density of TTC-STEG reaches 8.8 V/m^2 with 0.25-sun Xe light irradiation and is proportional to the increasing intensity of the light from 0.25 to 1 sun. The corresponding temperature of TTC-PU photothermal membrane rises to 70°C under 1-sun Xe light compared with 37°C of simulated skin, which demonstrates effectively augmented temperature gradient of TTC-STEG for high power generation. Furthermore, four cyclic

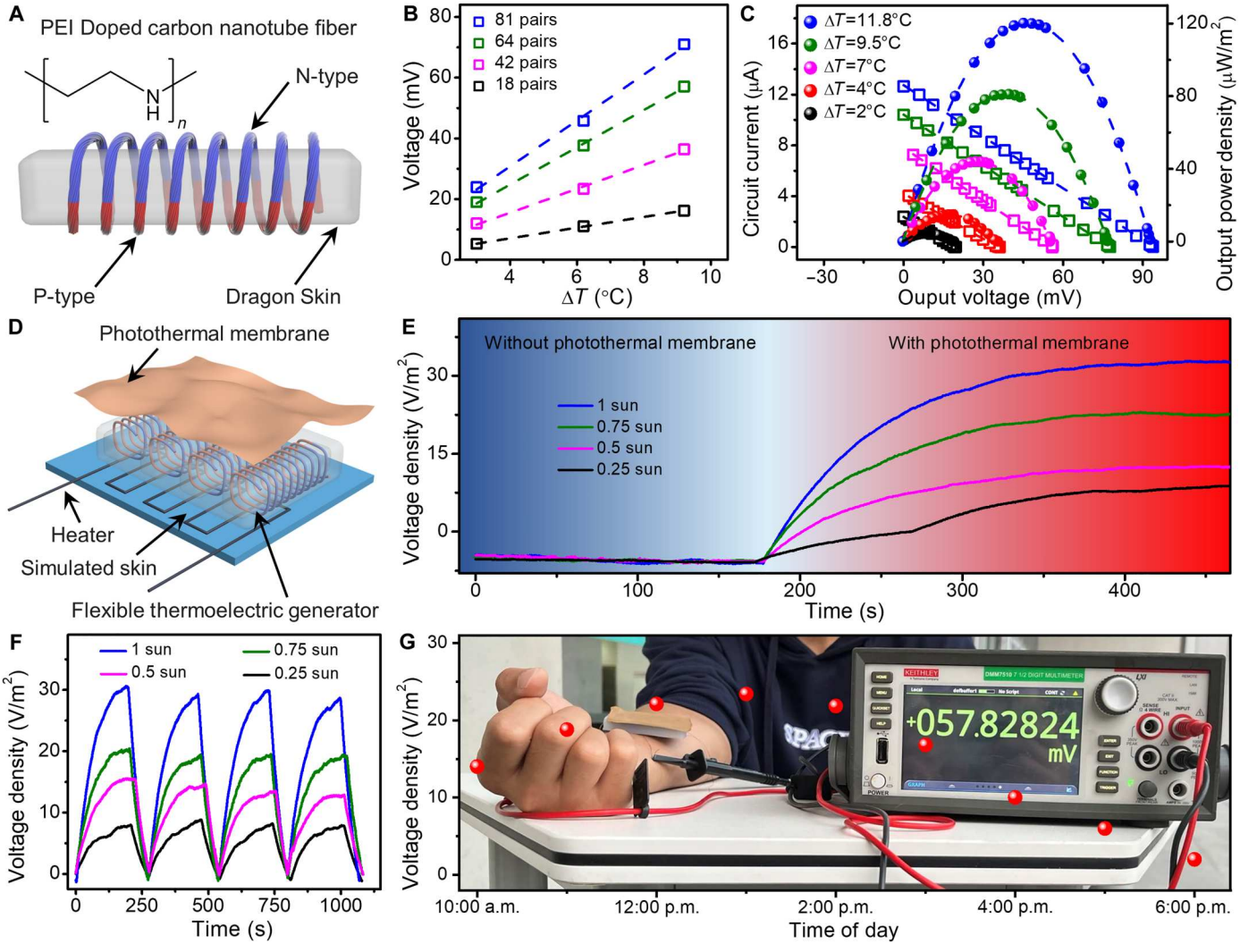

Fig. 5. TE properties of CNT-based TEG and output performance of TTC-STEG. (**A**) Schematic illustration of the fabrication process of the CNT-based TEG. (**B**) The variations in output voltage along with P-N pairs and Δ*T*. (**C**) The circuit current and output power density as a function of output voltage under different Δ*T*. (**D**) Schematic diagram of the TTC-STEG. (**E**) The output voltage density of TTC-STEG was tested under different Xe light intensities, and (**F**) corresponding cyclic tests. (**G**) The real-time voltage density data of TTC-STEG under natural light at Suzhou (China) on 24 October 2022.

tests were conducted under different Xe light intensities, which confirmed the outstanding stability of light collection and excellent conversion from heat to electricity (Fig. 5F). As shown in Fig. 5G and fig. S30, the output voltage density of the prepared TTC-STEG in direct contact with human skin under natural light was investigated from 10:00 a.m. to 6:00 p.m. The voltage density is consistent with the variation in solar irradiance, which reaches a maximum of 23.4 V/m^2 at 1:00 p.m. Substantially, the outdoor experiments profoundly confirm the excellent light harvesting of the stretchable TTC-PU photothermal membrane and the effective TE conversion of the flexible TTC-STEG. As a flexible and lightweight electronic device, TTC-STEG could sustainably and stably generate excellent TE power, demonstrating its enormous potential to be widely applied in wearable electronics. The power conversion performance of TTC-STEG under the condition of human body wearing with Xe light 1-sun intensity was conducted (fig. S31A). As displayed in fig. S31B, the circuit current decreases when the load resistance increases from 100 to 600,000 ohms, while the voltage of the external resistance exhibits the rising trend. Furthermore, the developed TTC-STEG demonstrates a maximum power density of 196 μW/m^2 when the internal resistance is equal to the external resistance (fig. S31C). Notably, the TTC-STEG with excellent optical concentrator of TTC-PU membrane achieves the Δ*T* of 33.0°C with 2-sun Xe light irradiation and holds the Δ*T* more than 2 hours (fig. S32), which is larger than that of other common heat source (table S5).

DISCUSSION

In summary, the flexible wearable STEGs with unique features of converting solar energy into electricity were devised. The donor TMBD and acceptor TCBQ were selected to rationally construct NIR-II absorption organic photothermal CT cocrystals via a self-assembly process. The electron delocalization from the HOMO of

TMBD to the LUMO of TCBQ contributes to a narrow energy gap of 1.5 eV and a wide absorption from 200 to 1950 nm. Fs-TA spectra demonstrate that the rapid nonradiative dynamic pathways of IC, ISC, and charge dissociation to the ground state favor the high PCE (80.5%) of the TTC cocrystal, which was further incorporated into a PU substrate to fabricate a stretchable photothermal nanofiber membrane via electrospinning technology. Furthermore, the TTC-PU photothermal membranes having a high PCE of 73.7% under the strain more than 80% were applied as stretchable optical concentrators that coat on the surface of the flexible CNT-based TE fibers to augment temperature gradient of 33°C for high TE power generation. The wearable TTC-STEG demonstrates a maximum output voltage density of 32.8 V/m^2 with 1-sun Xe light irradiation and 23.4 V/m^2 at 1:00 p.m. under natural light. Impressively, the stretchable and large-area photothermal membrane of NIR-II absorption TTC cocrystal for the larger temperature gradient of STEGs holds great sights in efficiently improving TE performance toward flexible wearable electronics.

MATERIALS AND METHODS

Materials

TMBD (CAS: 366-29-0) and TCBQ (CAS: 118-75-2) were purchased from TCI. Dichloromethane (DCM; analysis grade), *N*,*N*-dimethylformamide (DMF; analysis grade), PEI (analysis grade), and ethanol (analysis grade) were purchased from Beijing Chemical Ltd., China. All of the chemical compounds were directly used without further purification. The PU was purchased from Dongguan Haosheng New Materials Co. Ltd. The Dragon Skin 10 NV was purchased from Smooth-On Store. The CNT yarns were purchased from Suzhou Institute of Nano-Tech and Nano-Bionics, Chinese Academy of Sciences.

Fabrication of TTC cocrystal microrods

The TTC cocrystal microrods were prepared via a facile solution self-assembly process (*47*). Typically, 10 μmol (2.40 mg) of TMBD and 10 μmol (2.46 mg) of TCBQ were dissolved in 1 ml of DCM, obtaining the stock solution. Then, this stock solution was added into 1 ml of EtOH, the well-mixed solution was dropped onto a quartz substrate, and then TTC cocrystal microrods could be obtained dominantly when the solvents gradually evaporated.

Fabrication of TTC-PU photothermal nanofiber membrane

The TTC-PU photothermal nanofiber membrane was fabricated by electrospinning technology (JDF05) (*48*). Typically, 4.0 g of DMF and 6.0 g of DCM with the mass ratio of 4:6 were mixed in a glass bottle. Then, TTC cocrystal microrods and PU at the concentrations of 3 and 10 wt % were dissolved into mixed solution, followed by magnetic stirring overnight. Furthermore, the spinning solution collecting in syringe was pumped out by infusion pump at a rate of 1.2 ml/hour through a needle. The high voltage power supply is set to 25 kV. The TTC-PU photothermal nanofiber membrane was successfully fabricated until the spinning solution was sprayed completed.

TE properties of CNT yarns

The pristine CNT yarns are favorable P-type TE elements, which demonstrate a Seebeck coefficient of ~66 μV/K, an electrical conductivity of ~16246 S/m, and an average power factor of 70.77 μW/(m·K^2). The physical adsorption of PEI onto pristine CNTs converts them from P-type to N-type ascribed to the amine-rich polymer-donating electrons to the nanotubes. The influences of PEI adsorption on the Fermi energy shifting of pristine CNTs were evaluated according to the UV photoelectron spectroscopy (UPS) and the absorption spectra (fig. S33). The PEIs acting as donors shift the Fermi energy upward compared to its initial energy state, contributing to N-type behavior (*49*), which demonstrate a Seebeck coefficient of ~−65 μV/K, an electrical conductivity of ~18011 S/m, and an average power factor of 76.10 μW/(m·K^2). It demonstrates a successful doping method to prepare N-type TE elements. The electrical conductivity ρ was measured using the formula: the cross section of the fiber is considered circular, $\rho = L/(\pi r^2 R)$, where L, R, and r are the gauge length (10 cm), electric resistance, and mean radius of the tested gauge, respectively.

Characterizations

The morphology and size of the organic micro/nanostructures were examined by field-emission SEM (Hitachi, SU8010, Japan) dropping on an indium tin oxide–coated glass. The TEM images were obtained by a TEM (FEI company, Tecnai G2 F20, USA). One drop of the solution was dropped on a carbon-coated copper grid and evaporated. TEM measurement was conducted at room temperature at an accelerating voltage of 100 kV. The XRD patterns were measured by a D/max 2400 x-ray diffractometer with Cu Kα radiation (λ = 1.54050 Å) operated in the 2θ range from 5° to 50°, by using the samples on the quartz. The bright optical images and fluorescence images were recorded using a fluorescence optical microscope (Leica, DM4000M, Germany) with a spot-enhanced charge couple device (Diagnostic Instrument Inc.). The excitation source is a mercury lamp equipped with a band-pass filter (330 to 380 nm for UV light). The samples were fabricated by placing a drop of solution onto a cleaned quartz and then evaporated at room temperature. Micro-area PL spectra were obtained by a homemade optical microscopy. To measure the PL spectra of individual microrod, the microrod was excited locally with a 375-nm laser focused down to the diffraction limit. The excitation laser was filtered with a 375-nm notch filter. The light was subsequently coupled to a grating spectrometer (Princeton Instrument, ARC-SP-2356) and recorded by a thermal-electrically cooled charge-coupled device (Princeton Instruments, PIX-256E). The ESR experiments were carried out on a JES-X320 spectrometer. The ESR detection was conducted at a microwave frequency of 9.15 GHz and a microwave power of 1.0 mW at room temperature. The Raman spectra were analyzed by using a Raman spectrometer (HORIBA HR Evolution, France). The IR spectra were performed on an IR-408 (Shimadzu, Japan). The ^{13}C NMR spectra were conducted on an AVANCE III 400 machine (Bruker, Germany). The absorption spectra were analyzed with a UV3600 (Shimadzu, Japan). The Fs-TA measurements were performed on the basis of a femtosecond Ti:sapphire regenerative amplified laser system (Coherent, Astrella-Tunable-F-1k) and Fs-TA spectrometer system (Ultrafast Systems, Helios Fire). The stress-strain behavior was investigated by Instron 5967. TGA was conducted on TA Instruments SDT2960. Specific heat capacity results were obtained by the differential scanning calorimetry 2500 (*50*). The unknown specific heat capacity could be determined by the specific heat capacity of sapphire method. The xenon (Xe) lamp is CEL-PE300-4A. The recorded real-time solar irradiance was experimented on CEL-NP2000-Sun180. The open-circuit

voltage, short-circuit current, output power were measured by a multimeter (Keithley7510) and an electrometer (Keithley6514). The UPS was conducted on Thermo Fisher Scientific ESCALAB 250Xi.

Theoretical calculations

Crystal growth structure prediction was obtained by Materials Studio package. The theoretical calculations are carried out using the Gaussian 09 software packages. The geometries of the individual molecules were optimized at the B3LYP/6-31G (d,p) level. The ESP and excited state analysis were carried out by a wave function analysis tool Multiwfn (*51*). The 2D fingerprint plots were obtained using Crystal Explorer 21.

Supplementary Materials

This PDF file includes:
Supplementary Text
Figs. S1 to S33
Tables S1 to S5
Legend for movie S1

Other Supplementary Material for this manuscript includes the following:
Movie S1

REFERENCES AND NOTES

1. N. Xu, P. Zhu, Y. Sheng, L. Zhou, X. Li, H. Tan, S. Zhu, J. Zhu, Synergistic tandem solar electricity-water generators. *Joule* **4**, 347–358 (2020).
2. P. Zhu, C. Shi, Y. Wang, Y. Wang, Y. Yu, Y. Wang, Y. Deng, J. Xiao, Recyclable, healable, and stretchable high-power thermoelectric generator. *Adv. Energy Mater.* **11**, 2100920 (2021).
3. N. Komatsu, Y. Ichinose, O. S. Dewey, L. W. Taylor, M. A. Trafford, Y. Yomogida, G. Wehmeyer, M. Pasquali, K. Yanagi, J. Kono, Macroscopic weavable fibers of carbon nanotubes with giant thermoelectric power factor. *Nat. Commun.* **12**, 4931 (2021).
4. F. Suarez, A. Nozariasbmarz, D. Vashaee, M. C. Öztürk, Designing thermoelectric generators for self-powered wearable electronics. *Energy Environ. Sci.* **9**, 2099–2113 (2016).
5. Y. Zhang, K. Wu, Q. Fu, A structured phase change material with controllable thermo-conductive highways enables unparalleled electricity via solar-thermal-electric conversion. *Adv. Funct. Mater.* **32**, 2109255 (2022).
6. D. H. Lee, S. B. Pyun, Y. Bae, D. P. Kang, J.-W. Park, E. C. Cho, Solution-processed plasmonic–dielectric sunlight-collecting nanofilms for solar thermoelectric application. *ACS Appl. Mater. Interfaces* **9**, 43583–43595 (2017).
7. V. Padmanabhan Ramesh, Y. Sargolzaeiaval, T. Neumann, V. Misra, D. Vashaee, M. D. Dickey, M. C. Ozturk, Flexible thermoelectric generator with liquid metal interconnects and low thermal conductivity silicone filler. *npj Flex. Electron.* **5**, 5 (2021).
8. D. Kraemer, B. Poudel, H.-P. Feng, J. C. Caylor, B. Yu, X. Yan, Y. Ma, X. Wang, D. Wang, A. Muto, K. McEnaney, M. Chiesa, Z. Ren, G. Chen, High-performance flat-panel solar thermoelectric generators with high thermal concentration. *Nat. Mater.* **10**, 532–538 (2011).
9. C. Xin, Z. Hu, Z. Fang, M. Chaudhary, H. Xiang, X. Xu, L. Aigouy, Z. Chen, Flexible and wearable plasmonic-enabled organic/inorganic hybrid photothermoelectric generators. *Mater. Today Energy* **22**, 100859 (2021).
10. T. Fukui, S. Kawai, S. Fujinuma, Y. Matsushita, T. Yasuda, T. Sakurai, S. Seki, M. Takeuchi, K. Sugiyasu, Control over differentiation of a metastable supramolecular assembly in one and two dimensions. *Nat. Chem.* **9**, 493–499 (2017).
11. C. Wang, H. Dong, L. Jiang, W. Hu, Organic semiconductor crystals. *Chem. Soc. Rev.* **47**, 422–500 (2018).
12. M.-P. Zhuo, Y.-C. Tao, X.-D. Wang, Y. Wu, S. Chen, L.-S. Liao, L. Jiang, 2D organic photonics: An asymmetric optical waveguide in self-assembled halogen-bonded cocrystals. *Angew. Chem. Int. Ed.* **57**, 11300–11304 (2018).
13. X. Zhen, K. Pu, X. Jiang, Photoacoustic imaging and photothermal therapy of semiconducting polymer nanoparticles: Signal amplification and second near-infrared construction. *Small* **17**, e2004723 (2021).
14. J. Xu, Q. Chen, S. Li, J. Shen, P. Keoingthong, L. Zhang, Z. Yin, X. Cai, Z. Chen, W. Tan, Charge-transfer cocrystal via a persistent radical cation acceptor for efficient solar-thermal conversion. *Angew. Chem. Int. Ed.* **61**, e202202571 (2022).
15. B. Kim, H. Shin, T. Park, H. Lim, E. Kim, NIR-sensitive poly(3,4-ethylenedioxyselenophene) derivatives for transparent photo-thermo-electric converters. *Adv. Mater.* **25**, 5483–5489 (2013).
16. B. Lü, Y. Chen, P. Li, B. Wang, K. Müllen, M. Yin, Stable radical anions generated from a porous perylenediimide metal-organic framework for boosting near-infrared photothermal conversion. *Nat. Commun.* **10**, 767 (2019).
17. H. Wang, K.-F. Xue, Y. Yang, H. Hu, J.-F. Xu, X. Zhang, In situ hypoxia-induced supramolecular perylene diimide radical anions in tumors for photothermal therapy with improved specificity. *J. Am. Chem. Soc.* **144**, 2360–2367 (2022).
18. S. Liu, X. Zhou, H. Zhang, H. Ou, J. W. Y. Lam, Y. Liu, L. Shi, D. Ding, B. Z. Tang, Molecular motion in aggregates: Manipulating TICT for boosting photothermal theranostics. *J. Am. Chem. Soc.* **141**, 5359–5368 (2019).
19. X. Ye, L.-H. Chung, K. Li, S. Zheng, Y.-L. Wong, Z. Feng, Y. He, D. Chu, Z. Xu, L. Yu, J. He, Organic radicals stabilization above 300 °C in Eu-based coordination polymers for solar steam generation. *Nat. Commun.* **13**, 6116 (2022).
20. W. Du, Y. Chong, X. Hu, Y. Wang, Y. Zhu, J. Chen, X. Li, Q. Zhang, G. Wang, J. Jiang, G. Liang, Increasing photothermal efficacy by simultaneous intra- and intermolecular fluorescence quenching. *Adv. Funct. Mater.* **30**, 1908073 (2020).
21. W. Zhu, R. Zheng, Y. Zhen, Z. Yu, H. Dong, H. Fu, Q. Shi, W. Hu, Rational design of charge-transfer interactions in halogen-bonded co-crystals toward versatile solid-state optoelectronics. *J. Am. Chem. Soc.* **137**, 11038–11046 (2015).
22. S. K. Park, I. Cho, J. Gierschner, J. H. Kim, J. H. Kim, J. E. Kwon, O. K. Kwon, D. R. Whang, J.-H. Park, B.-K. An, S. Y. Park, Stimuli-responsive reversible fluorescence switching in a crystalline donor–acceptor mixture film: Mixed stack charge-transfer emission versus segregated stack monomer emission. *Angew. Chem. Int. Ed.* **55**, 203–207 (2016).
23. S. Horiuchi, F. Ishii, R. Kumai, Y. Okimoto, H. Tachibana, N. Nagaosa, Y. Tokura, Ferroelectricity near room temperature in co-crystals of nonpolar organic molecules. *Nat. Mater.* **4**, 163–166 (2005).
24. Y. D. Zhao, J. Han, Y. Chen, Y. Su, Y. M. Cao, B. Wu, S. M. Yu, M.-D. Li, Z. Wang, M. Zheng, M.-P. Zhuo, L.-S. Liao, Organic charge-transfer cocrystals toward large-area nanofiber membrane for photothermal conversion and imaging. *ACS Nano* **16**, 15000–15007 (2022).
25. Y.-T. Chen, M.-P. Zhuo, X. Wen, W. Chen, K.-Q. Zhang, M.-D. Li, Organic photothermal cocrystals: Rational design, controlled synthesis, and advanced application. *Adv. Sci.* **10**, 2206830 (2023).
26. L. Sun, W. Zhu, X. Zhang, L. Li, H. Dong, W. Hu, Creating organic functional materials beyond chemical bond synthesis by organic cocrystal engineering. *J. Am. Chem. Soc.* **143**, 19243–19256 (2021).
27. J.-R. Wu, D. Li, G. Wu, M.-H. Li, Y.-W. Yang, Modulating supramolecular charge-transfer interactions in the solid state using compressible macrocyclic hosts. *Angew. Chem. Int. Ed.* **61**, e202210579 (2022).
28. M. Yang, I. S. Park, T. Yasuda, Full-color, narrowband, and high-efficiency electroluminescence from boron and carbazole embedded polycyclic heteroaromatics. *J. Am. Chem. Soc.* **142**, 19468–19472 (2020).
29. Y. Xu, H. Yao, L. Ma, L. Hong, J. Li, Q. Liao, Y. Zu, J. Wang, M. Gao, L. Ye, J. Hou, Tuning the hybridization of local exciton and charge-transfer states in highly efficient organic photovoltaic cells. *Angew. Chem. Int. Ed.* **59**, 9004–9010 (2020).
30. F. Kagawa, S. Horiuchi, M. Tokunaga, J. Fujioka, Y. Tokura, Ferroelectricity in a one-dimensional organic quantum magnet. *Nat. Phys.* **6**, 169–172 (2010).
31. M.-P. Zhuo, Y. Yuan, Y. Su, S. Chen, Y.-T. Chen, Z.-Q. Feng, Y.-K. Qu, M.-D. Li, Y. Li, B.-W. Hu, X.-D. Wang, L.-S. Liao, Segregated array tailoring charge-transfer degree of organic cocrystal for the efficient near-infrared emission beyond 760 nm. *Adv. Mater.* **34**, e2107169 (2022).
32. E. R. Johnson, S. Keinan, P. Mori-Sánchez, J. Contreras-García, A. J. Cohen, W. Yang, Revealing noncovalent interactions. *J. Am. Chem. Soc.* **132**, 6498–6506 (2010).
33. J. Zhang, L. Hu, K. Zhang, J. Liu, X. Li, H. Wang, Z. Wang, H. H. Y. Sung, I. D. Williams, Z. Zeng, J. W. Y. Lam, H. Zhang, B. Z. Tang, How to manipulate through-space conjugation and clusteroluminescence of simple AIEgens with isolated phenyl rings. *J. Am. Chem. Soc.* **143**, 9565–9574 (2021).
34. Y. Wang, W. Zhu, W. Du, X. Liu, X. Zhang, H. Dong, W. Hu, Cocrystals strategy towards materials for near-infrared photothermal conversion and imaging. *Angew. Chem. Int. Ed.* **57**, 3963–3967 (2018).
35. W. Zhu, L. Zhu, Y. Zou, Y. Wu, Y. Zhen, H. Dong, H. Fu, Z. Wei, Q. Shi, W. Hu, Deepening insights of charge transfer and photophysics in a novel donor–acceptor cocrystal for waveguide couplers and photonic logic computation. *Adv. Mater.* **28**, 5954–5962 (2016).
36. L. Sun, W. Zhu, W. Wang, F. Yang, C. Zhang, S. Wang, X. Zhang, R. Li, H. Dong, W. Hu, Intermolecular charge-transfer interactions facilitate two-photon absorption in styrylpyridine–tetracyanobenzene cocrystals. *Angew. Chem. Int. Ed. Engl.* **56**, 7831–7835 (2017).
37. H. Xiang, Q. Yang, Y. Gao, D. Zhu, S. Pan, T. Xu, Y. Chen, Cocrystal strategy toward multifunctional 3D-printing scaffolds enables NIR-activated photonic osteosarcoma hyperthermia and enhanced bone defect regeneration. *Adv. Funct. Mater.* **30**, 1909938 (2020).

38. Y. Wang, H. Wu, W. Zhu, X. Zhang, Z. Liu, Y. Wu, C. Feng, Y. Dang, H. Dong, H. Fu, W. Hu, Cocrystal engineering: Toward solution-processed near-infrared 2D organic cocrystals for broadband photodetection. *Angew. Chem. Int. Ed.* **60**, 6344–6350 (2021).
39. X. Li, L. Liu, S. Li, Y. Wan, J.-X. Chen, S. Tian, Z. Huang, Y.-F. Xiao, X. Cui, C. Xiang, Q. Tan, X.-H. Zhang, W. Guo, X.-J. Liang, C.-S. Lee, Biodegradable π-conjugated oligomer nanoparticles with high photothermal conversion efficiency for cancer theranostics. *ACS Nano* **13**, 12901–12911 (2019).
40. J. Guo, H. Ohkita, H. Benten, S. Ito, Near-IR femtosecond transient absorption spectroscopy of ultrafast polaron and triplet exciton formation in polythiophene films with different regioregularities. *J. Am. Chem. Soc.* **131**, 16869–16880 (2009).
41. F. Etzold, I. A. Howard, R. Mauer, M. Meister, T.-D. Kim, K.-S. Lee, N. S. Baek, F. Laquai, Ultrafast exciton dissociation followed by nongeminate charge recombination in PCDTBT: PCBM photovoltaic blends. *J. Am. Chem. Soc.* **133**, 9469–9479 (2011).
42. M. Segal, M. A. Baldo, M. K. Lee, J. Shinar, Z. G. Soos, Frequency response and origin of the spin-1/2 photoluminescence-detected magnetic resonance in a π-conjugated polymer. *Phys. Rev. B* **71**, 245201 (2005).
43. X. Lu, Y. Hu, J. Guo, C.-F. Wang, S. Chen, Fiber-spinning-chemistry method toward in situ generation of highly stable halide perovskite nanocrystals. *Adv. Sci.* **6**, 1901694 (2019).
44. R. Cheng, Z.-B. Liang, L. Zhu, H. Li, Y. Zhang, C.-F. Wang, S. Chen, Fibrous nanoreactors from microfluidic blow spinning for mass production of highly stable ligand-free perovskite quantum dots. *Angew. Chem. Int. Ed.* **61**, e202204371 (2022).
45. W.-Z. Song, X.-X. Wang, H.-J. Qiu, N. Wang, M. Yu, Z. Fan, S. Ramakrishna, H. Hu, Y.-Z. Long, Single electrode piezoelectric nanogenerator for intelligent passive daytime radiative cooling. *Nano Energy* **82**, 105695 (2021).
46. Z. Soleimani, S. Zoras, B. Ceranic, Y. Cui, S. Shahzad, A comprehensive review on the output voltage/power of wearable thermoelectric generators concerning their geometry and thermoelectric materials. *Nano Energy* **89**, 106325 (2021).
47. I. Adams, G. M. Bancroft, Solution evaporation method for solid state ESCA studies. *Nature* **250**, 219–220 (1974).
48. T. Wu, H. Li, J. Xue, X. Mo, Y. Xia, Photothermal welding, melting, and patterned expansion of nonwoven mats of polymer nanofibers for biomedical and printing applications. *Angew. Chem. Int. Ed.* **58**, 16416–16421 (2019).
49. J. L. Blackburn, A. J. Ferguson, C. Cho, J. C. Grunlan, Carbon-nanotube-based thermoelectric materials and devices. *Adv. Mater.* **30**, 1704386 (2018).
50. A. K. Galwey, Crystal chemistry and molecular mechanisms in molten magmas: The significance of fusion in reactions of solids. *Thermochim. Acta* **269-270**, 621–630 (1995).
51. T. Lu, F. Chen, Multiwfn: A multifunctional wavefunction analyzer. *J. Comput. Chem.* **33**, 580–592 (2012).

Acknowledgments

Funding: We appreciate the financial support of the National Natural Science Foundation of China (52203234 and 51873134), Priority Academic Program Development of Jiangsu Higher Education Institutions (PAPD), Natural Science Foundation of Jiangsu Province of China (BK20211317), Opening Project of China National Textile and Apparel Council Key Laboratory of Silk Functional Materials and Technology of Soochow University, Opening Project of National Engineering Laboratory for Modern Silk, Jiangsu Jiangnan High Polymer Fiber Co. Ltd., "111" Project of the State Administration of Foreign Experts Affairs of China, and Jiangsu Naton Science & Technology Co. Ltd. **Author contributions:** Conceptualization: Y.D.Z., M.-P.Z., and Z.-S.W. Methodology: M.-P.Z. and Z.-S.W. Investigation: Y.D.Z., W.J., and S.Z. Visualization: B.W. and P.L. Supervision: M.Z., J.H., and W.C. Writing—original draft: Y.D.Z., M.-P.Z., and K.-Q.Z. Writing—review and editing: Y.D.Z., M.-P.Z., and L.-S.L. **Competing interests:** The authors declare that they have no competing interests. **Data and materials availability:** All data needed to evaluate the conclusions in the paper are present in the paper and/or the Supplementary Materials.

Submitted 22 March 2023
Accepted 24 August 2023
Published 13 December 2023
10.1126/sciadv.adh8917